Composite Structures 94 (2012) 3538–3545

Contents lists available at SciVerse ScienceDirect

Composite Structures

journal homepage: www.elsevier.com/locate/compstruct

Dynamic fracture of graphite/epoxy composites stiffened by buffer strips: An experimental study

Dongyeon Lee [a], Hareesh Tippur [a,*], Phillip Bogert [b]

[a] Department of Mechanical Engineering, Auburn University, AL 36849, United States
[b] NASA Langley Research Center, Hampton, VA 44313, United States

ARTICLE INFO

Article history:
Available online 7 June 2012

Keywords:
Graphite/epoxy
PETI-5/IM7
Stiffener
Dynamic fracture
Impact loading
Digital image correlation

ABSTRACT

Fracture responses of unidirectional graphite/epoxy composite coupons enhanced by buffer strips are investigated under impact loading conditions using digital image correlation technique and high-speed photography. Composite coupons made of phenylethynyl terminated imide oligomer (PETI-5) as matrix and IM7 graphite fiber as reinforcement are studied. Buffer strips are made of the same material but with a different stacking sequence to attain quasi-isotropy. Edge-notched coupons are subjected to impact loading along the axis of symmetry. The effectiveness of methods used for attaching the buffer strip, namely, co-curing at elevated temperatures and adhesive bonding at room temperature, are also examined. The optically measured stress intensity factor histories reveal that both methods provide nearly identical fracture responses. However, the crack initiates much later in coupons stiffened using adhesive bonding method than its co-cured counterpart and thus shows higher stress intensity factor at initiation. The residual stresses are shown to be responsible for the difference in the fracture responses.

1. Introduction

With the increasing use of fiber reinforced composites in primary aerospace structures, it is crucial that mechanical integrity of these be thoroughly studied and understood. One of the major concerns regarding these structures is their inherent weakness for catastrophic damage propagation along weak fiber/matrix interfaces during service [1–6]. A common design approach to mitigate such failures and improve damage tolerance [7] is to use crack-arresting buffer strips that alter the overall stiffness and fracture toughness favorably.

The stiffeners in composite structures also add to damage tolerance between structural inspection schedules. Among other factors, an inspection interval is dependent upon the fracture behavior of the material. However, due to the complex mechanical behavior of fiber reinforced composites, reliable determination of inspection intervals is challenging. In order to reduce uncertainty, crack arresters are typically installed at critical locations to delay damage propagation until the next scheduled inspection.

The reported studies on stiffened composite structures are relatively few and are carried out under static loading conditions. Sendeckyj [8] developed a crack arrestment criterion for cracked composite panels when cracks were in the main panel stiffened by strips of material. A limited validation of the criteria based on the reported experimental data was attempted with reasonable success. Gurdal and Haftka [9] developed an automated fracture mechanics based procedure for designing minimum weight composite panels subjected to a local damage constraint when loaded in tension. They coupled their scheme with a weight minimization approach and obtained results for both unstiffened and stiffened configurations. Sawicki et al. [10] experimentally investigated the ability of stiffeners to redirect a propagating damage in graphite/epoxy panels when subjected to uniaxial tension. They used photoelastic coatings to visualize shear strain contours and compare the results with the ones obtained using finite element analysis of the same geometry. They concluded that at failure, the propagating damage progressed across the stiffener and was controlled by the maximum tensile strain.

In the present study, stiffened composite panels made of both high-toughness material and crack-arresting buffer strips are experimentally evaluated under impact loading conditions. To the authors' knowledge, this is the first of its kind experimental study of dynamic fracture of stiffened composites. Unidirectional fiber-reinforced composites made of IM7 carbon fiber impregnated with PETI-5 are studied in this work. The role of crack-arresting buffer strips made of the same material but with different lay-up sequence installed perpendicular to the fiber orientation is investigated. Cracked composite coupons are subjected to impact loading and the resulting crack tip displacement fields are monitored optically and fracture parameters are extracted.

* Corresponding author.
E-mail address: htippur@eng.auburn.edu (H. Tippur).

0263-8223/$ - see front matter © 2012 Elsevier Ltd. All rights reserved.
http://dx.doi.org/10.1016/j.compstruct.2012.05.032

2. Experimental procedure

2.1. Materials

The composite material used in this study is IM7/PETI-5,[1] provided by NASA Langley Research Center, VA. The matrix material has a unique combination of properties including superior mechanical properties and thermal stability, excellent resistance to aircraft fluids, and easy processing in an autoclave. The details regarding its chemical composition and processing are available in an earlier paper [11]. Two lay-up sequences were used to manufacture sample sheets. The main panel was composed of 35 plies with fibers aligned in each ply in one direction (i.e., $[0]_{35}$). The crack-arresting buffer strips ('stiffener' in short hereafter) was composed of four plies, in which the stacking sequence was 90°/45°/-45°/0° in order to realize quasi-isotropy. The elastic material properties of the unidirectional laminate as well as those for quasi-isotropic laminate are listed in Table 1. The ones for the latter were computed based on unidirectional laminate properties using the approach of Tsai [12].

2.2. Specimen preparation

Two types of stiffened composite sheets were received with stiffeners attached on opposite sides: (a) stiffeners co-cured along with the main panel (Type A) and (b) stiffeners adhesively bonded using epoxy adhesive film – Scotch-Weld™ Structural Adhesive Film AF 555–0.08 Wt. (~300 μm thickness, storage modulus ~3 GPa at 25 °C) from 3 M (Type B).[2] Rectangular specimens (see, Fig. 1) were then cut from the sheet so that stiffeners were located 10 mm away from the top edge to avoid impact occurring directly on the stiffener. The specimen was 200 mm long and 50 mm wide. Type A specimen had a 5-mm thick main panel and was 6.2-mm thick in the stiffened region whereas Type B was 5.6-mm thick on the main panel and 8.2-mm thick in the stiffened region. (The thickness difference in the stiffeners was related to the availability of material than a specific design purpose.) The stiffener in both types of specimens was 15-mm wide. The fiber orientation was 0° relative to the short side of the specimen and coincided with the loading direction. A pre-notch was made on the bottom edge of the specimen, parallel to fiber orientation, using a diamond impregnated wafer blade resulting in a notch with approximately 300 μm tip. The notch tip was manually sharpened using a razor blade. The pre-notch was examined under a microscope for crack tip bluntness and direction. The crack tip was rather sharp, approximately 5 μm in crack-tip radius. Further, the pre-notch was found well aligned with respect to the fiber orientation and perpendicular to the bottom edge, eliminating the possibility of mode-II fracture if the loading axis was made collinear with the notch. The schematic in Fig. 1 shows all other dimensions of the coupon studied.

The reinforcement was symmetric with respect to the mid-plane of the main panel in terms of mass as well as the stacking sequence. Thus only in-plane deformations were dominant during impact loading, and no other fracture mode was excited at the macro scale.

In order to utilize the digital image correlation method, the coupons were sprayed with black and white paint to create random speckle patterns. The typical speckle size and optical magnification of the camera was such that on average each speckle covered 4–6 pixels of the imaging array of the camera. The mean value of the recorded gray scale ranged between 100 and 120 on a 0–255 scale. The histogram of the recorded gray scale had an approximate Gaussian distribution. These are shown to produce a measurement resolution of approximately 3 μm [14,15] in the current experimental setup.

[1] Phenylethynyl terminated imide oligomers fifth composition.

[2] AF 555 is a thermosetting, modified epoxy film. The film can be co-cured, co-bonded with composite prepregs, or used to bond cured composite. The film adhesive can be cured from 150ºC up to 180 °C.

Table 1
Elastic properties of the material used in the study.

	Unidirectional [13]	Quasi-isotropic
E_1 (GPa)	151.7	57.12
E_2 (GPa)	9.65	57.12
G_{12} (GPa)	4.14	21.58
ν_{12}	0.33	0.324
d (kg/m^3)	1580	–

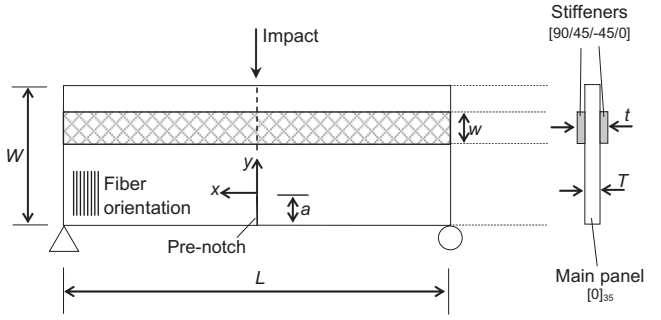

Fig. 1. Schematic of sample geometry used: $W = 50$, $L = 200$, $T = 5$ for Type A and 5.6 for Type B, $t = 6.2$ for Type A and 8.2 for Type B, and $w = 15$. All units are in mm. Lay-up sequence of stiffeners is symmetric with respect to mid-plane of main panel. Although the schematic of experimental loading condition in this figure indicates 3-point bending, in reality 1-poing impact tests were done since crack initiation and propagation occurred before stress waves reflected back from the supports/anvils to the crack tip.

2.3. Test procedure

Using a 2D Digital Image Correlation (DIC) technique, random speckles on a specimen surface were monitored during the transient impact event. The speckle patterns were photographed before and after deformation in the region-of-interest. The deformed speckle images corresponding to the fracture event were paired with the ones recorded prior to loading and analyzed. During the analysis, a sub-image within the undeformed image was chosen, and the location of its counterpart in the deformed image was sought. Once identified, the local displacement components of the sub-image were quantified. In the current work, an approach developed by Kirugulige et al. [14,15] and Lee et al. [16] was used to estimate in-plane 2D displacement components. The region-of-interest was approximately 40×40 mm^2 (1000×1000 in pixel) and sub-image size is 26 pixels × 26 pixels, which generated a 37×37 displacement vector grid.

After evaluating the displacement fields, u_x and u_y, linear elastic fracture mechanics was used to extract fracture parameters. The displacement components u_x and u_y in the vicinity of crack tip subjected to mixed mode (mode-I and -II) loading are expressed as [17]:

$$\begin{aligned} u_x &= K_I\sqrt{\frac{2r}{\pi}}\mathrm{Re}\left[\frac{1}{\mu_2-\mu_1}(p_1\mu_2 z_1 - p_2\mu_1 z_2)\right] \\ &\quad + K_{II}\sqrt{\frac{2r}{\pi}}\mathrm{Re}\left[\frac{1}{\mu_2-\mu_1}(p_1 z_1 - p_2 z_2)\right] + \cdots \\ u_y &= K_I\sqrt{\frac{2r}{\pi}}\mathrm{Re}\left[\frac{1}{\mu_2-\mu_1}(q_1\mu_2 z_1 - q_2\mu_1 z_2)\right] \\ &\quad + K_{II}\sqrt{\frac{2r}{\pi}}\mathrm{Re}\left[\frac{1}{\mu_2-\mu_1}(q_1 z_1 - q_2 z_2)\right] + \cdots \end{aligned} \tag{1}$$

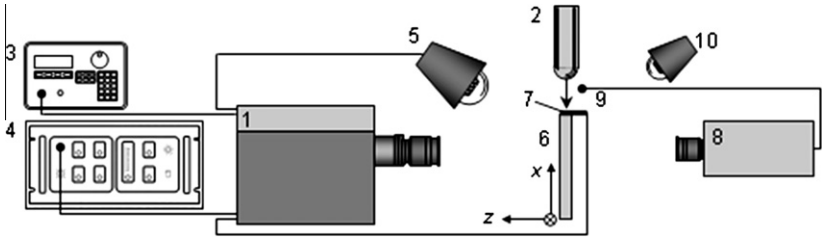

Fig. 2. Schematic of the experimental setup: (1) Cordin 550 high-speed digital camera, (2) impact tup of the drop tower, (3) delay generator, (4) Cordin lamp control unit, (5) a pair of Cordin light sources, (6) specimen, (7) copper tape, (8) Phantom v710 high-speed digital camera, (9) optical sensor, (10) LED lamps for Phantom high-speed camera.

where K_I and K_{II} are mode-I and -II stress intensity factors and quantities p_j, q_j, and z_j are defined as

$$p_j = \mu_j^2 s_{11} + s_{12} - \mu_j s_{16}$$

$$q_j = \mu_j s_{12} + \frac{s_{22}}{\mu_j} - s_{26}$$

$$z_j = \sqrt{\cos\theta + \mu_j \sin\theta}$$

and μ_j ($j = 1, 2$) are the two roots with positive imaginary part of the equation

$$s_{11}\mu^4 - 2s_{16}\mu^3 + (2s_{12} + s_{66})\mu^2 - 2s_{26}\mu + s_{22} = 0 \qquad (2)$$

where s_{ij} are the elements of the compliance matrix.

The coordinate x, one of two principal directions of a composite sample, is parallel to pre-notch length and y is perpendicular to it. The polar coordinates r and θ are the radial distance from the crack tip and the angle relative to the x-axis, respectively. Note that Eq. (1) hold for static loading conditions or in situations before crack initiation for impact loading conditions. In the latter case, the inertial effects enter the coefficients of the asymptotic fields, namely, the crack tip stress intensity factors. As demonstrated in Lee et al. [18], transient effects associated with crack-tip velocity are minimal when the crack-tip velocity is significantly lower than shear wave speed of the material.[3] In view of this, transient terms associated with crack growth were not considered during data analysis.

2.4. Experimental setup

The dynamic fracture tests were carried out by subjecting specimens to symmetric impact loading. By measuring displacement fields in the crack tip vicinity using the 2D digital image correlation method and high-speed photography, the evolution of dynamic fracture parameters during stress-wave loading was quantified. The schematic of the experimental set-up used in these tests is shown in Fig. 2. It consisted of an Instron Dynatup 9250-HV drop tower for delivering low-velocity impact (impact velocity = 4.85 m/s, mass = 5 kg) and a Cordin-550 multi-sensor (32 CCD sensors each of 1000 × 1000 pixel spatial resolution) high-speed digital camera for capturing gray-scale speckle images. The drop tower had an instrumented tup for recording the impact force history and a pair of anvils for recording support reaction histories. The set-up also included a delay/trigger generator to produce a trigger pulse with an appropriate time delay when the tup contacted the specimen. In view of the short duration transient event, two high-intensity flash lamps were used to illuminate the specimen surface. Typically the illumination lasted one millisecond. Since the high-speed camera had a limit in terms of recording time window (in this work, it was a maximum of 320 μs depending on the framing rate chosen), a second high-speed camera (Phantom v710 by Vision Research, a single CMOS sensor, 1280 × 960 pixel spatial resolution) was also utilized. The second high-speed camera allowed recording the event for a longer duration but at a substantially lower spatial resolution (208 × 200 pixels). This enabled photography for over one full second at varying framing rates. The operation of both of the cameras was synchronized in order to track critical failure events such as time at impact, crack initiation time after impact, and total duration for fracture. An optical sensor was placed in the path of the impactor to trigger the camera when the moving tup tripped the light beam emitted by the sensor. The location of the sensor was determined so that the Phantom high-speed camera was triggered slightly ahead of the Cordin high-speed camera. The framing rate in this study varied between 100,000–250,000 frames/s providing an inter-frame rate duration of 10–4 μs, respectively.

3. Results

Tests were divided into three different groups based on the stiffener bonding method used and the specimens without stiffeners. As noted previously, stiffeners for Type A and B were prepared differently. Type C was an unstiffened panel to provide a control experiment. Multiple experiments, six of Type A, three of Type B, and three of Type C were carried out.

A few selected images for a Type A sample are shown in Fig. 3 along with the corresponding measured displacement fields. These images and the measured fields were from the Cordin camera. As evident from the photographs, after impact the crack suffers deformation and initiates from the initial notch tip propagating towards the stiffener. The crack tip stays at the edge of stiffener until the stiffener is completely fractured. This was confirmed by the low-resolution high-speed camera (Phantom camera) images, to be presented later on. The ability of the stiffener to momentarily arrest the crack tip is evident from Fig. 3d. The time window recorded by the high-speed camera in this case was from 45 to 200 μs. Since images were not available beyond 200 μs, the Phantom camera operated simultaneously to photograph the back side of the specimen to provide *qualitative* information regarding subsequent fracture events in the vicinity of the stiffener. The events corresponding to different stages of failure (Fig. 3) are as follows:

(a) (40 μs). Pre-crack initiation phase: The longitudinal wave speed for the material in the fiber direction being ~10,000[4] m/s, the stress waves have arrived and strain energy has accumulated at the crack tip.

[3] Based on the values in Table 1, the shear wave speed for IM7/PETI5 is ~1600 m/s. In the current study, the crack-tip velocity ranged between 500 and 600 m/s and was less than 40% of the material shear wave speed.

[4] The longitudinal wave speed for the material in the fiber direction here was computed from the relationship, $c_l = \sqrt{c_{11}/\rho}$ in which c_l indicates the longitudinal wave speed, c_{11} one of the stiffness matrix elements, and ρ the material density.

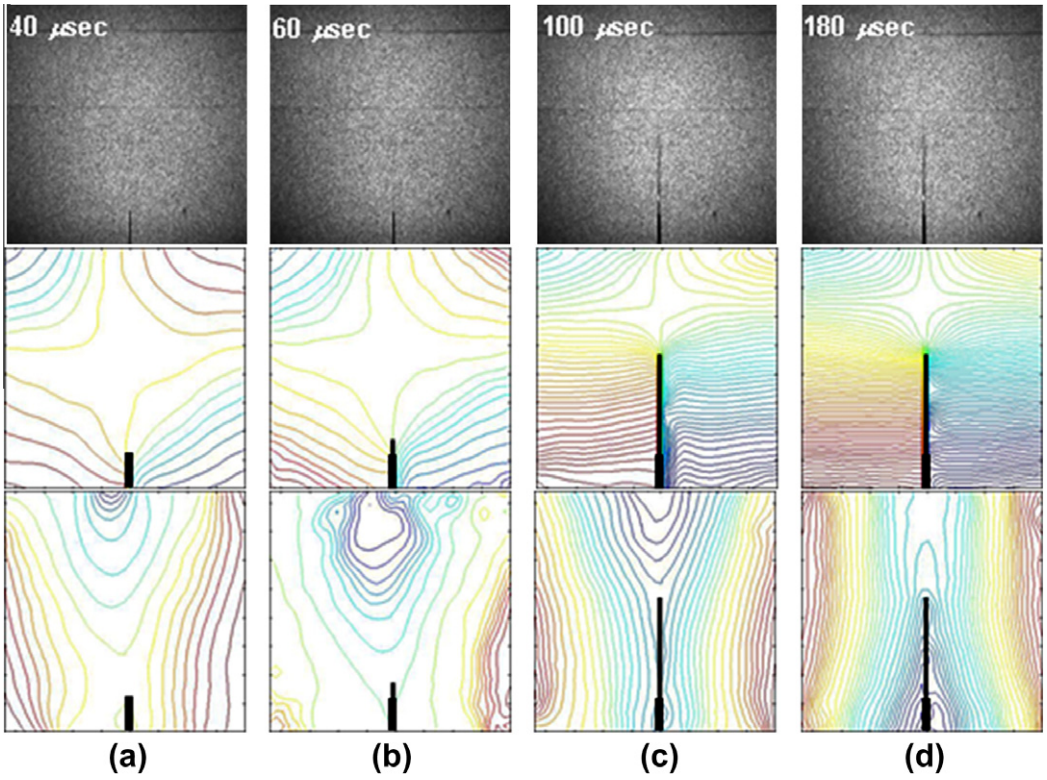

Fig. 3. Displacement fields corresponding to a few select speckle images (first row) for Type A (stiffened IM7/PETI-5, co-cured): The measured opening displacement in the 2nd row and sliding displacement in the 3rd row. Contour intervals are 5 micrometers.

(b) (60 μs). Crack initiation occurs and the initial crack-tip velocity is about 430 m/s. (The crack velocity was obtained from finite difference approximation of crack length measured between two consecutive images.)
(c) (100 μs). Corresponds to post-crack initiation phase; The crack propagates in a self-similar fashion towards the stiffener reaching its lower edge. The crack continues to open resulting in a monotonic increase of SIF.
(d) (180 μs). The stiffener arrests the crack tip; The SIF values reach a plateau.

A typical sequence of failure events for Type B coupons subjected to impact loading is shown in Fig. 4. Once again, crack propagation can be described for different stages as follows:

(a) (30 μs). Corresponds to pre-crack initiation period.
(b) (100 μs). The crack initiation occurs.
(c) (135 μs). The crack tip grows towards the stiffener and is halted there until a *se*condary initiation occurs.
(d) (180 μs). The crack tip SIF continues to increase and potentially enters a plateau value as in Type A coupons. (This could not be confirmed as photography ended in each of the successful experiments.)

The differences in various times between Type A and B specimens will be discussed later on.

As noted earlier, the Phantom high-speed camera images were recorded and utilized beyond the time window of the Cordin camera. The intention here was to capture the images of crack arrested by the stiffener. As evident in Fig. 5, the crack indeed is arrested momentarily at the lower edge of the stiffener. Based on the Phantom camera images, the crack tip remained stationary for ~400 μs. The SIF values extracted from the DIC attained a peak value of ~13.9 MPa $(m)^{1/2}$ for Type A coupons and continued relatively unchanged due to crack arrest. Due to the unavailability of optical data, SIF values at this stage for Type B coupons could not be evaluated. Approximately 700–800 μs after the crack reached the lower edge of the stiffener, the crack propagation resumed into the stiffener, causing its failure and eventually the failure of the coupon was complete at ~900 μs.

The SIF history evaluated from an over-deterministic least-squares analysis of displacement fields [19] for Type A coupons is shown in Fig. 6a for three specimens. The average crack initiation time is ~63 μs after impact and the average mode-I SIF at initiation ($K_{I\text{-}ini}$), is 3.85 ± 0.48 MPa $(m)^{1/2}$. It is noteworthy that the SIF continuously increases past crack initiation up to ~14 MPa $(m)^{1/2}$. Type B coupons produced a crack initiation toughness of 4.55 ± 0.20 MPa $(m)^{1/2}$ at an average time of ~97 μs as shown in Fig. 6b. This is a considerable improvement when compared to the Type A coupons.

The stress intensity factor at initiation for three different Type C (unstiffened) coupons was an average of 2.5 ± 0.49 MPa $(m)^{1/2}$ and crack initiation time was ~105 μs after impact. Interestingly, these values are similar the ones (~2.0 MPa $(m)^{1/2}$ and ~110 μs) reported by the authors in Ref. [11] for the same material system but prepared in a different batch. Although some experimental scatter was observed in the three responses, they showed a similar tendency, namely a monotonic increase in SIF up to crack initiation and a continued but small increase past crack initiation up to a peak value followed by a modest drop off in the SIF history. Note that all the graphs are not plotted here in favor of brevity.

A comparison of SIF histories from all three different types of coupons is made in Fig. 7. The SIF histories for each type were averaged and plotted. One can readily see that the magnitude of SIF at initiation for both of the stiffened coupons is higher than that of unstiffened counterpart. Thus, regardless of the bonding method used, stiffeners indeed improve the dynamic fracture performance

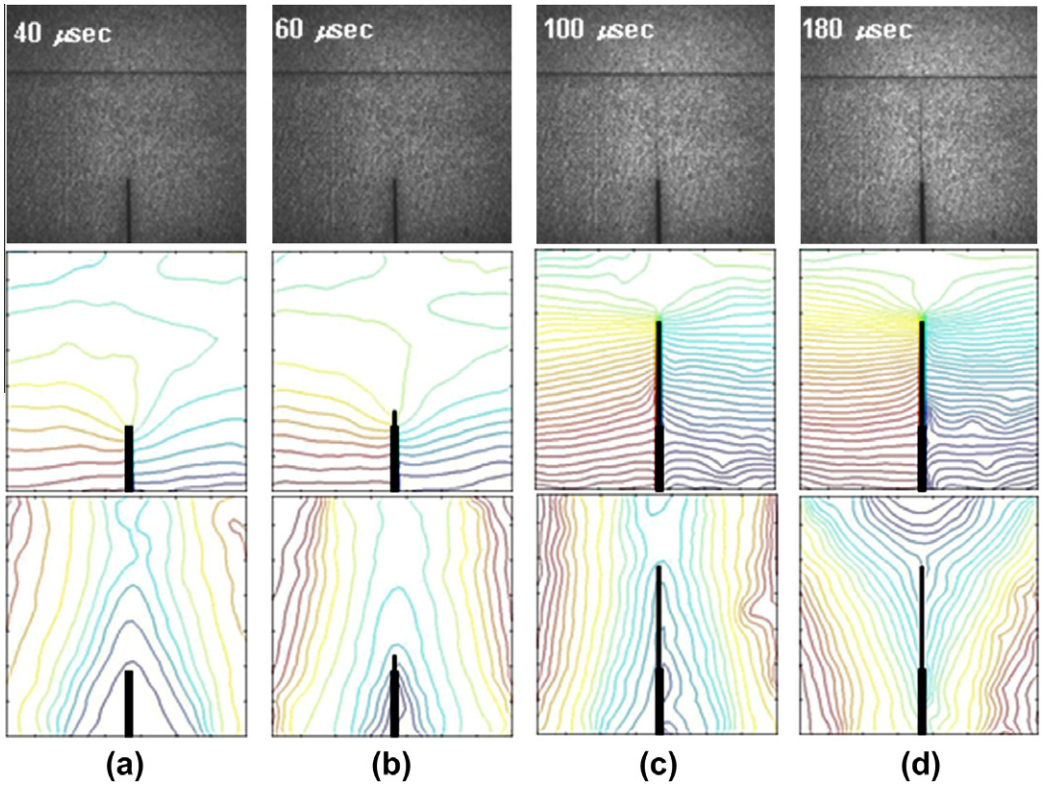

Fig. 4. Displacement fields corresponding to a few select speckle images (first row) for Type B (stiffened IM7/PETI-5, adhesively bonded): The measured opening displacement in the 2nd row and sliding displacement in the 3rd row. Contour intervals are 5 μm.

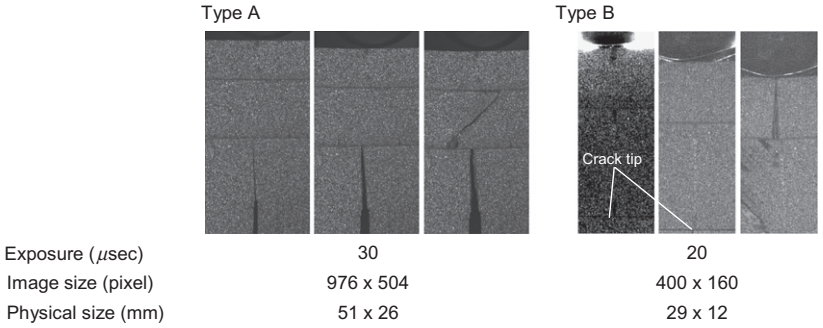

Fig. 5. Phantom high-speed camera images for Type A and Type B coupons. For each type, the first image represents instant when the crack tip reaches bottom edge of the stiffener, second image represents the crack just before stiffener failure, and third image when the crack propagates across the stiffener. The time interval between first and second images is 400 μs for both cases.

of the main panel. The improvement in stress intensity factor at crack initiation is more than 50% relative to the unstiffened coupons. After crack initiation, the crack growth resistance in stiffened coupons is more evident considering that the SIF for Type C reached its peak value at ~3.2 MPa $(m)^{1/2}$ as opposed to the SIF histories for both Type A and B coupons which show an increase to approximately 12–14 MPa $(m)^{1/2}$. It is also noteworthy that the SIF histories for the two stiffened specimen types are nearly identical except for the crack initiation time. Despite the lack of experimental data at later stages in case of Type B specimens, the trend of this plot strongly suggests that the SIF continuously rise after crack initiation, very similar to the pattern seen with Type A coupons. However, the crack initiated substantially earlier, at ~34 μs, for the Type B coupons when compared to ~97 μs in Type A cases. This issue will be addressed in the ensuing section.

4. Premature crack initiation in co-cured coupons

Although the overall fracture performance of Type A and B stiffened coupons seem quite similar, the early crack initiation in the latter relative to the former (and the unstiffened panels – Type C – case) was a concern and demanded further investigation. Among the various possibilities, the potential for residual stresses was suspected and investigated. NASA Langley researchers had previously reported that, despite the improvement in performance against crack propagation, the stiffeners could significantly increase residual stress compared to unstiffened composite panels [20]. In order to assess and quantify the presence of residual stresses, a slitting method [21] used in conjunction with an optical deformation mapping approach was used. Although this method does not provide details regarding residual stress components like the popular

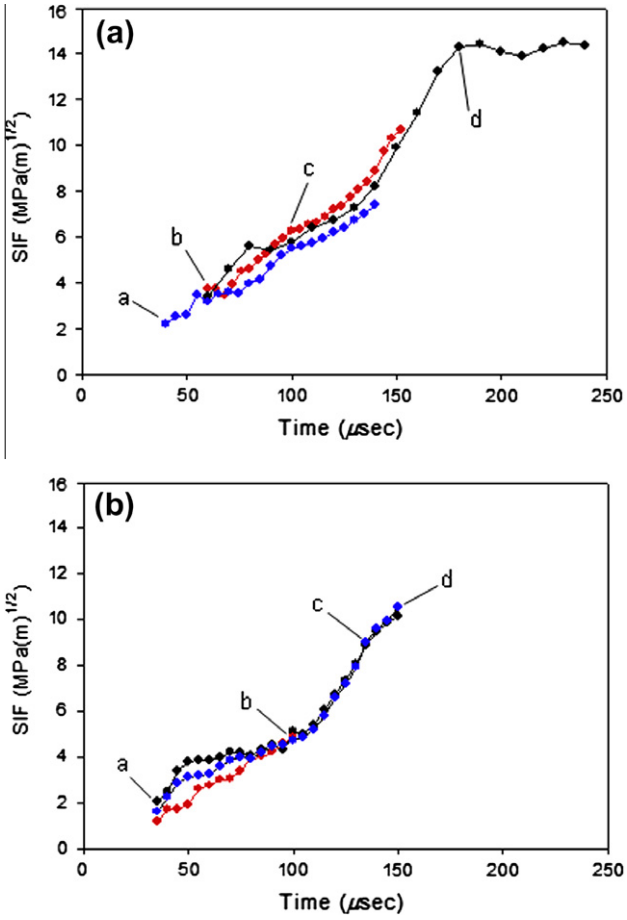

Fig. 6. Stress intensity factor histories for a few Types A and B unidirectional IM7/PETI-5 composite specimens.

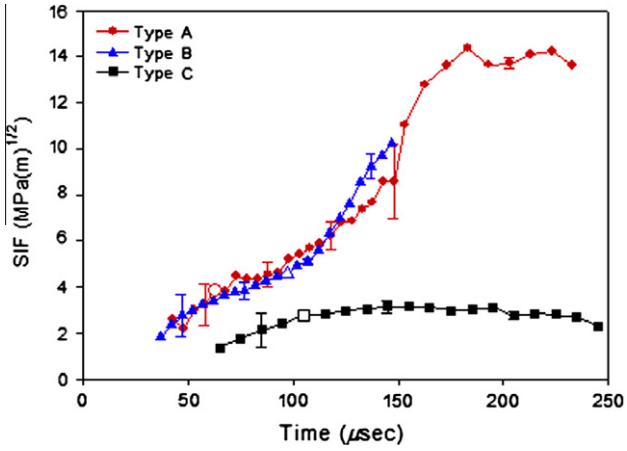

Fig. 7. Comparison of measured SIF histories for Type A (stiffened, co-cured), Type B (stiffened, glued) and Type C (unstiffened) unidirectional IM7/PETI-5 composite specimens. The open symbol in each plot denotes crack initiation.

hole-drilling approach, it does reveal on the presence of residual stresses and its estimated influence on SIF at crack initiation.

Rectangular coupons were cut out of Type A and Type B stiffened panels and decorated with black and white speckles, as described earlier. The stiffener location relative to the two long edges of the specimen was maintained the same as in the previously described fracture experiments. The specimen was mounted on a 3D translation stage and gripped along the line-of-symmetry in the stiffened region. Fig. 8 shows the actual experimental set-up used. A diamond impregnated circular saw blade mounted on the shaft of a variable-speed motor was used for slitting the specimen. A pair of white light sources and a digital SLR camera (Nikon D100) fitted with a long focal length lens and an extension tube was used to record the decorated speckles during slitting operation. A reference image was photographed prior to the start of the cutting process. Using the translation stage, the specimen was slowly fed (at approximately 2 mm/min) towards the rotating saw to create a notch along the axis-of-symmetry. The speckle images were recorded at regular slit length intervals to be used as 'deformed' images for subsequent DIC analysis.

The speckle images from the deformed and reference states were correlated and displacement fields were extracted. Type B specimens, irrespective of the length of the slit, showed no discernible deformation of the specimen. However, in Type A specimens, as the length of the slit increased, the specimen deformations (sliding and opening displacement components) were significant and increased monotonically, indicating the presence of residual stresses. An example of the measured displacement fields are shown in Fig. 9 along with the 'deformed' speckle field on the specimen. This image corresponds to the stage when the crack propagated without assistance when a critical crack length was reached. Although the newly initiated hair-line crack tip is not visible in the photographed image, it is clearly evident in the crack opening displacement field. That is, a crack has grown from the notch/slit tip, evident as the discontinuity in crack opening displacement field well ahead of the notch tip. (The slit tip and the crack tip are highlighted as solid circles in Fig. 9.)

The crack sliding and opening displacement contours in the immediate vicinity of the crack tip show a great deal of similarity to that expected in the case of a dominant mode-I crack. In the far-field, however, slight asymmetry in the number of contours above and below the crack line in the sliding displacement field and non-perpendicular crack opening displacement contours behind the crack tip are evident. These deviations can be attributed to possible crack face friction, asymmetric residual stress released during notch insertion and/or sample clamping during slit insertion. Despite these deviations, an over-deterministic least-squares analysis using mixed-mode displacement fields for an orthotropic material was undertaken for *estimating* the SIF values at various notch lengths using measured displacements in the notch tip vicinity. The analysis produced a relatively negligible mode-II SIF (approximately 10%) when compared to the mode-I counterpart at each slit length. The estimated mode-I SIF variation as the slit length was increased is shown in Fig 10. Two coupons with co-cured stiffener (Type A) and one coupon with glued stiffener (Type B) were tested. Evidently, in Type A coupons as the notch length was increased, the measured SIF ($K_{\text{I-slit}}$) increased monotonically (from ~0.5 to 3.0 MPa $(\text{m})^{1/2}$ over a slit length range of 4–9 mm) until reaching a critical value at which a self-similar crack growth occurred in the unloaded specimens without further effort. This is evident as a distinct drop in $K_{\text{I-slit}}$ values in Fig. 10. On the contrary, for the specimen with glued stiffeners, SIFs are negligibly small (~0.2 MPa $(\text{m})^{1/2}$) at different notch lengths, and are well within the margin of error expected in the least-squares analysis of displacement fields acquired from DIC. The fact that the glued coupons did not show significant deformations upon the introduction of the slit (and hence negligible mode-I SIF values) over ~20 mm notch length strongly points to the co-curing of the stiffener with the main panel as the source of the residual stresses in Type A coupons. Further, this was attributed to the coefficient of thermal expansion (CTE) mismatch between the quasi-isotropic stiffener and the unidirectional base-panel during co-curing under elevated temperature and pressure. It should also be noted that Type B spec-

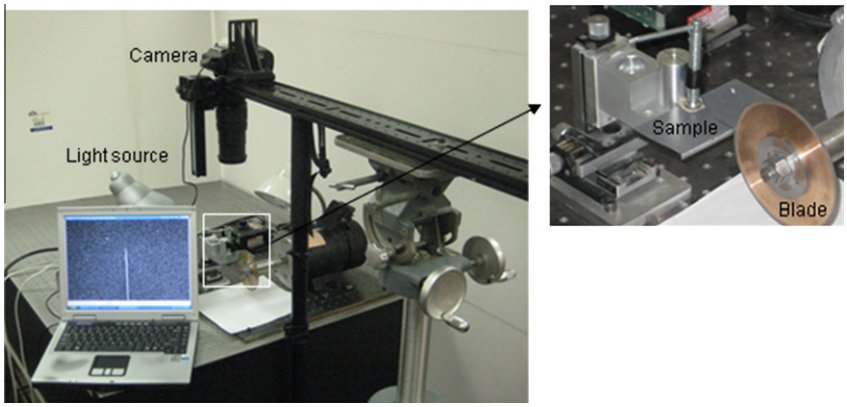

Fig. 8. Experimental set-up for the study of residual stress estimation consisting of a wafering blade, two white light sources, a camera mounted on a tripod, and a computer for data acquisition.

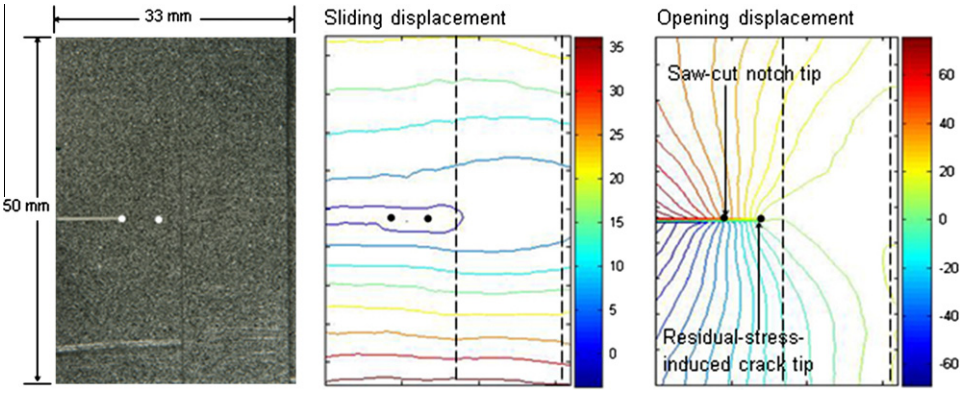

Fig. 9. Measured displacement fields immediately after crack initiation with the photographed speckle image. Dotted lines indicate the area occupied by the stiffener. The solid symbols denote the slit tip and the self-propagated crack tip.

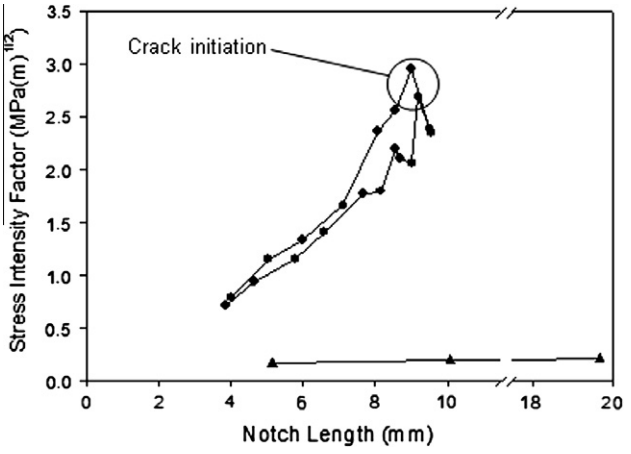

Fig. 10. Residual mode-I stress intensity factor (KI-slit) for two Type A (filled circles, stiffened, co-cured) and one Type B (filled triangles; stiffened, glued) coupons during cutting process.

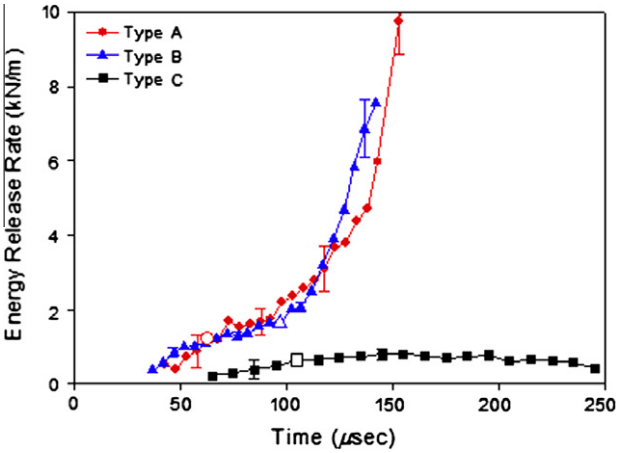

Fig. 11. Comparison of average energy release rate histories for all three types of stiffened and unstiffened IM7/PETI-5 coupons. Open symbols correspond to crack initiation.

imens, where the stiffeners were adhesively affixed to the main panel at room temperature, do not suffer from the CTE mismatch issue and hence showed crack initiation occurring at much later times (close to that seen in unstiffened coupons).

The energy release rate is another quantity that provides an informative description of a material's fracture performance. The total energy release rate (G_{total}) that causes crack initiation could have contributions from mechanical loading (G_m) and residual stresses (G_r) in such that [22]:

$$G_{total} = G_m + G_r \tag{3}$$

This assertion can be verified using energy release rate histories plotted for Type A, B and C coupons, shown in Fig. 11. Type A cou-

pons had a critical G_r of ~1.20 kN/m at crack initiation and that for Type C specimen, under load experienced crack initiation at ~0.60 kN/m. The sum of these two values is approximately 1.80 kN/m. On the other hand, energy release rate for Type B, representing G_{total}, is ~1.60 kN/m, close to the sum of the energy release rates G_r and G_m, supporting the possibility of the residual stresses in Type A coupons. It should be noted that the residual stresses perhaps may have contributed adversely to the situation in the current case due to the unidirectional panel layup with a quasi-isotropic stiffener.

5. Conclusions

Unidirectional IM7/PETI-5 carbon fiber-reinforced composites stiffened with buffer strips made of the same material were fracture-tested under mode-I impact loading conditions. Stiffeners were attached to the main panel using two different methods, co-curing and film-adhesive bonding. The test sample surface was decorated with black and white speckles in order to implement digital image correlation technique to measure full-field in-plane displacement fields during dynamic fracture events. The test samples were categorized into three groups: Co-cured stiffened composite coupons (Type A), adhesively bonded composite coupons (Type B), and composite coupons without stiffeners (Type C). The primary results of this work are itemized as follows:

1. A nearly identical SIF history was observed for both co-cured and adhesively bonded stiffener cases. However, crack initiation in coupons with co-cured stiffeners occurred considerably earlier than that for adhesively bonded counterparts.
2. The crack initiated in the adhesively bonded stiffener and unstiffened cases at approximately the same time after impact. The crack initiation time for coupons with co-cured stiffener, on the other hand, was approximately 60% of that for the other two cases.
3. The SIF at crack initiation for co-cured stiffener specimens was ~3.85 MPa $(m)^{1/2}$ whereas it was ~4.55 MPa $(m)^{1/2}$ for adhesively bonded stiffener specimens, about 18% higher.
4. Based on previous observations in conclusions 1–3, presence of residual stress was suspected in the co-cured stiffener specimens due to CTE mismatch between the main panel and the stiffener during material processing.
5. Residual stress estimation using a slitting method was undertaken to measure SIF corresponding to self-sustained crack initiation/growth in the absence of loading due to residual stresses. The SIF at crack initiation in these tests was found to be ~2.85 MPa $(m)^{1/2}$, compared to the value of 2.50 MPa $(m)^{1/2}$ obtained for unstiffened samples.
6. Unlike coupons with stiffeners produced by co-curing process, adhesively bonded stiffeners did not show presence of significant residual stresses.
7. Both types of stiffened composite showed a good ability to arrest a dynamically growing crack.

Acknowledgment

This research was sponsored by the NASA-LaRC under cooperative agreement No. NNX07AC64B.

References

[1] Erdogan F, Ozbek T. Stresses in fiber-reinforced composites with imperfect bonding. ASME-Paper 69-WA/APM-15; 1969.
[2] Chamis CC. Mechanics of load transfer at the interface. Compos Mater 1974:31–77.
[3] Outwater JO, Murphy JC. On the catastrophic failure of laminated structures. In: Society of the plastics industry, reinforced plastics/composites institute, annual conference – proceedings; 1974.
[4] Kendall K. Interfacial cracking of a composite – 1. Interlaminar shear and tension. J Mater Sci 1976;11(4):638–44.
[5] Johnson P, Chang F-K. Characterization of matrix crack-induced laminate failure – Part I: Experiments. J Compos Mater 2001;35(22):2009–35.
[6] Johnson P, Chang F-K. Characterization of matrix crack-induced laminate failure – Part II: Analysis and verifications. J Compos Mater 2001;35(22):2037–74.
[7] Dastin SJ, Erbacher HA. Experiences with Composite Aircraft Structures. In: National SAMPE Symposium and Exhibition (Proceedings); 1980. p. 706–15.
[8] Sendeckyj GP. Concepts of crack arrestment in composites, fracture mechanics of composites. Philadelphia: ASTM STP 593, American Society for Testing and Materials; 1975. p. 215–26.
[9] Gurdal Z, Haftka RT. Design of stiffened composite panels with a fracture constraint. Comput Struct 1985;20(1–3):457–65.
[10] Sawicki AJ, Graves MJ, Lagace PA. Failure of graphite/epoxy panels with stiffening strips, vol. 4. Philadelphia: ASTM STP 1156, American Society for Testing and Materials; 1993. p. 5–34.
[11] Lee D, Tippur H, Jensen BJ, Bogert P. Tensile and Fracture Characterization of PETI-5 and IM7/PETI-5 Graphite/Epoxy Composites under Quasi-Static and Dynamic Loading Conditions. J Eng Mater Technol, Trans ASME 2011;133(2):021015.
[12] Tsai S, Hahn HT. Introduction to Composite Materials. Technomic Publishing Co., Inc.; 1980.
[13] Ural A, Zehnder A, Ingraffea A. Fracture mechanics approach to facesheet delamination in honeycomb: measurement of energy release rate of the adhesive bond. Eng Fract Mech 2003;70(1):93–103.
[14] Kirugulige MS, Tippur HV, Denney TS. Measurement of transient deformations using digital image correlation method and high-speed photography. Appl Opt 2007;46(24):5083–96.
[15] Kirugulige MS, Tippur HV. Measurement of surface deformations and fracture parameters for a mixed-mode crack driven by stress waves using image correlation technique and high-speed photography. Strain 2009;45(2):108–22.
[16] Lee D, Tippur HV, Kirugulige MS, Bogert P. Experimental study of dynamic crack growth in unidirectional graphite/epoxy composite using digital image correlation method and high-speed photography. J Compos Mater 2008;43(19):2081–108.
[17] Sih GC, Paris PC, Irwin GR. On cracks in rectilinearly anisotropic bodies. Int J Fract 1965;1:189–203.
[18] Lee D, Tippur HV, Bogert P. Quasi-static and dynamic fracture of graphite/epoxy composites: an optical study of loading-rate effects. Compos Part B: Eng 2010;41(6):462–74.
[19] Sanford RJ. Application of the least-squares method to photoelastic analysis. Exp Mech 1980;20(6):192–7.
[20] Poe Jr CC, Kennedy JM. An assessment of buffer strips for improving damage tolerance of composite laminates. J Compos Mater 1980;14(1):57–70.
[21] Blair A, Daynes N, Hamilton D, Horne G, Heard PJ, Hodgson DZL, et al. Residual stress relaxation measurements across interfaces at macro- and micro-scales using slitting and DIC. In: Journal of physics: conference series, 7th international conference on modern practice in stress and vibration analysis, vol. 181(1); 2009. p. 012078.
[22] Liu C, Rosakis AJ, Stout MG. Dynamic fracture toughness of a unidirectional graphite/epoxy composite. In: Am soc mech eng appl mech div AMD (ASME-IMECE 2001), dynamic failure in composite materials and structures, New York; 11–19 November, 2001. p. 1–12.